Earthq Eng & Eng Vib (2016) 15: 697-714 **DOI**:10.1007/s11803-016-0359-4

Stiffness degradation-based damage model for RC members and structures using fiber-beam elements

Guo Zongming†, Zhang Yaoting‡, Lu Jiezhi† and Fan Jian§

School of Civil Engineering and Mechanics, Huazhong University of Science and Technology, Wuhan 430074, China

Abstract: To meet the demand for an accurate and highly efficient damage model with a distinct physical meaning for performance-based earthquake engineering applications, a stiffness degradation-based damage model for reinforced concrete (RC) members and structures was developed using fiber beam-column elements. In this model, damage indices for concrete and steel fibers were defined by the degradation of the initial reloading modulus and the low-cycle fatigue law. Then, section, member, story and structure damage was evaluated by the degradation of the sectional bending stiffness, rod-end bending stiffness, story lateral stiffness and structure lateral stiffness, respectively. The damage model was realized in Matlab by reading in the outputs of OpenSees. The application of the damage model to RC columns and a RC frame indicates that the damage model is capable of accurately predicting the magnitude, position, and evolutionary process of damage, and estimating story damage more precisely than inter-story drift. Additionally, the damage model establishes a close connection between damage indices at various levels without introducing weighting coefficients or force-displacement relationships. The development of the model has perfected the damage assessment function of OpenSees, laying a solid foundation for damage estimation at various levels of a large-scale structure subjected to seismic loading.

Keywords: fiber beam-column element; stiffness degradation; damage index; reinforced concrete column; reinforced concrete frame

1 Introduction

As an important component of performance-based seismic engineering, structural damage analysis has become a topic of considerable interest in the field of civil engineering. In recent decades, various analytical damage models (Park and Ang, 1985; Ghobarah, 2001; Hindi and Sexsmith, 2001; Heo, 2009; Yazgan and Dazio, 2012) for RC members and RC structures have been proposed, and several of these damage models are currently being applied in actual projects. Usually a damage model quantifies the damage magnitude with a damage index, which is expressed as a function of one response parameter or functions of certain response parameters, such as stress, displacement, ductility, stiffness, hysteretic energy, or fatigue characteristics.

One of the commonly used parameters of a degradation-based model is stiffness, which allows for a direct description of the mechanical characteristics of a material, a section, an element and a structure. Thus, stiffness-based damage models can be used to assess the damage at all the above-mentioned levels. In addition, as the initial and degraded stiffness of members can be detected by dynamic testing methods (Maas *et al.*, 2012), stiffness-based damage models can be verified at the section level and member level without considerable difficulty. Various stiffness-based damage models have been proposed in the literature (Ghobarah *et al.*, 1999; Kunnath *et al.*, 1997). Recently, Li *et al.* (2013) evaluated the damage of an RC member and frame by introducing damaged hinges and plastic hinges to capture their stiffness degradation behavior. From the existing literature, it can be concluded that the existing stiffness-based damage models can evaluate member, structure, and even section damage, but the connection between damage at these levels is not clear. In addition, to the authors' knowledge, it is assumed by nearly all of the existing stiffness-based damage models that damage is concentrated in certain specific regions of a member, and embodied by introducing plastic hinges or other types of hinges. However, due to the randomness of structural parameters and earthquake excitations, the damage location also possesses uncertainty. Thus, existing stiffness-based damage models may provide an inaccurate assessment of the local damage to a member, which would make it difficult to determine the failure paths of a member or structure and predict the failure modes of a structure. Different from the aforementioned assumption, fiber beam-column

Correspondence to: Zhang Yaoting, School of Civil Engineering and Mechanics, Huazhong University of Science and Technology, Wuhan 430074, China
Tel: +86-13517253167; Fax: +86-27-87542231
E-mail: zyt1965@mail.hust.edu.cn
†PhD Candidate; ‡Professor; §Assistant Professor

Supported by: the National Natural Science Foundation of China under Grant Nos. 51278218 and 51078166
Received June 4, 2015; **Accepted** December 27, 2015

elements allow for inelastic behavior to spread throughout the entire element (Calabrese *et al.*, 2010), and therefore, the latter problem is expected to be solved by introducing fiber elements into damage analysis.

In the fiber beam-column model, the response of a given cross-section can be derived by integrating the inelastic material response over the section (Kostic and Filippou, 2012). The element inelasticity is then obtained by integrating the contribution provided by each section (Calabrese *et al.*, 2010); then, the response of members and structures can be obtained sequentially. Thus, the definition of the fiber damage index is the cornerstone of the damage model using fiber beam-column elements, and determining how to establish the connection between the various levels of damage indices is the main task. To define the damage index of a concrete fiber, concrete stress, fracture parameter, initial reloading modulus have been introduced. To define the damage index of a steel fiber, steel strain and the low-cycle fatigue law have been adopted. Though fiber damage can be defined sensibly and monitored experimentally, the connection between the various levels of damage indices may not be established rationally for the frequent use of the artificially defined weighting coefficient method (Heo, 2009; Li *et al*., 2014), maximum/minimum value method (Teng *et al*., 2011; Li *et al*., 2011; Amziane and Dubé, 2008) and average value method (Tsuchiya and Maekawa, 2006). These methods not only destroy the link between damage indices and their physical meaning, but also introduce considerable uncertainty during damage transformations, especially from member level to story level and from story level to structure level.

To overcome the limitations of the existing damage models, this study developed a damage model using stiffness degradation and fiber beam-column elements simultaneously. Meanwhile, the direct stiffness method and static condensation method were used during damage transformations. Finally, the proposed damage model was applied to RC columns and an RC structure that were monitored under cyclic loading and seismic loading to assess their damage states and verify the reliability of the damage model.

2 Damage model based on stiffness degradation

In this study, the simplified Chang and Mander concrete model (Chang and Mander, 1994; Waugh, 2011) and the reinforcing steel model modified by Mazzoni *et al.* (2006) were applied to characterize the mechanical behavior of concrete and reinforcing bars. As shown in Fig. 1, the finite element program Opensees (Open System for Earthquake Engineering Simulation), which incorporates the aforementioned constitutive models, was used to perform the nonlinear analysis and export the stress-strain recorders of concrete and steel fibers by "record" command. Then the stress-strain recorders were read into Matlab by its "load" command, and fiber, section, member and structure damage indices were calculated sequentially by the proposed damage model realized in Matlab. In the damage model developed, the damage to the concrete fibers was defined by the degradation of the initial reloading modulus, and the damage to the reinforcing steel fibers was described by the low-cycle fatigue law. All of the fiber damage indices were calculated by custom functions. Then, section damage was evaluated by the degradation of the sectional bending stiffness, including the contributions of the damaged fibers. Next, the effective section stiffness was transformed to effective element stiffness using the force-based method, and the effective element stiffness was transformed into effective member stiffness corresponding to the degree of freedom of the rod-end using the direct stiffness method and static condensation method. The member damage index was defined by the degradation of the rod-end bending stiffness. Finally, story and structure damage was estimated by the degradation of the story lateral stiffness and structure lateral stiffness, which were obtained by the static condensation method. The concept based on stiffness degradation permeated the definitions of all levels of damage indices.

2.1 Damage to concrete fibers

To describe the damage to a concrete fiber, the constitutive model of a concrete fiber under uniaxial loading (Fig. 2) is expressed as

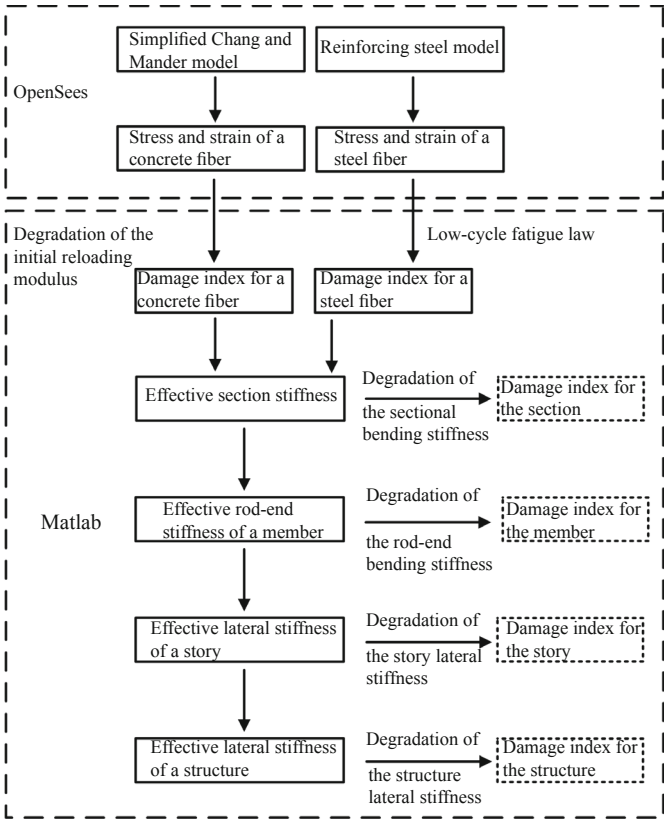

Fig. 1 Flowchart for deriving damage indices at various levels

$$\sigma_c = (1-D_c)\cdot E_c\cdot\left(\varepsilon_c-\varepsilon_c^p\right) \tag{1}$$

where σ_c is the concrete stress, ε_c and ε_c^p are the total and plastic concrete strain, respectively, E_c is the initial tangent modulus of concrete, and D_c is the concrete damage index.

According to Eq. (1), the damage index $D_{c,i}$ for the ith concrete fiber is defined as

$$D_{c,i}=1-\frac{\tilde{E}_{c,i}}{E_{c,i}} \tag{2}$$

where $E_{c,i}$ and $\tilde{E}_{c,i}$ are the initial tangent modulus and initial reloading modulus of the ith concrete fiber (Fig. 2), respectively.

In this study, the simplified Chang and Mander concrete model was chosen to simulate the hysteretic behavior of both confined and unconfined concrete fibers. In this constitutive model, the initial tangent modulus of concrete is expressed as follows (Chang and Mander, 1994):

$$E_c = 8\,200(f_c')^{3/8}\ \text{MPa} \tag{3}$$

where f_c' is the peak stress for unconfined concrete in MPa.

In the concrete model, the initial reloading modulus $\tilde{E}_c$ in tension and compression can be expressed as follows (Chang and Mander, 1994):

$$\tilde{E}_c=\frac{\left|\dfrac{f_{un}^-}{E_c\cdot\varepsilon_{cc}}\right|+0.57}{\left|\dfrac{\varepsilon_{un}^-}{\varepsilon_{cc}}\right|+0.57}\cdot E_c \qquad \text{for compression}$$

$$\tilde{E}_c=\frac{\left|\dfrac{f_{un}^+}{E_c\cdot\varepsilon_t}\right|+0.67}{\left|\dfrac{\varepsilon_{un}^+}{\varepsilon_t}\right|+0.67}\cdot E_c \qquad \text{for tension} \tag{4}$$

where ε_{cc} and ε_t are the concrete strain at the peak compressive stress and peak tensile stress, respectively, f_{un}^- and ε_{un}^- are the unloading stress and unloading strain from the compressive envelope curve, respectively, while f_{un}^+ and ε_{un}^+ are the unloading stress and unloading strain from the tension envelope curve, respectively.

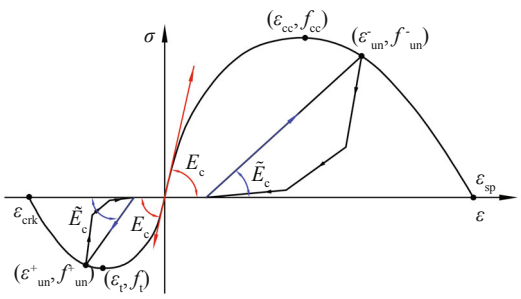

Fig. 2 Simplified Chang and Mander concrete model

Substituting Eqs. (3) and (4) into Eq. (2), the damage index of the ith concrete fiber can be derived as

$$D_{c,i}=1-\frac{\left|\dfrac{f_{un}^-}{8200(f_c')^{3/8}\cdot\varepsilon_{cc}}\right|+0.57}{\left|\dfrac{\varepsilon_{un}^-}{\varepsilon_{cc}}\right|+0.57} \qquad \text{for compresion}$$

$$D_{c,i}=1-\frac{\left|\dfrac{f_{un}^+}{8200(f_c')^{3/8}\cdot\varepsilon_t}\right|+0.67}{\left|\dfrac{\varepsilon_{un}^+}{\varepsilon_t}\right|+0.67} \qquad \text{for tension} \tag{5}$$

and assuming that $D_{c,i}=1$ when $\varepsilon_{un}^-<\varepsilon_{sp}$ or $\varepsilon_{un}^+<\varepsilon_{crk}$, where ε_{sp} is the spalling strain in compression and ε_{crk} is the cracking strain in tension.

2.2 Damage to reinforcing steel fibers

In the present study, the simplified equation proposed by Koh and Stephens (1991) was used to estimate the low-cycle fatigue life of a reinforcing steel fiber:

$$\varepsilon_a=\frac{\Delta\varepsilon}{2}=\frac{\varepsilon_{s,max}-\varepsilon_{s,min}}{2}=\varepsilon_f'(2N_f)^c \tag{6}$$

where ε_a is the strain amplitude, $\Delta\varepsilon$ is the total strain range, $\varepsilon_{s,max}$ and $\varepsilon_{s,min}$ are the maximum and minimum strains in a cycle, respectively, ε_f' is the fatigue ductility coefficient, $2N_f$ is the number of half-cycles to failure, and c is the fatigue ductility exponent.

By substituting Eq. (6) into Miner's linear damage accumulation rule (Miner, 1945), the damage to a reinforcing steel fiber due to ductility exhaustion is obtained:

$$D_{s,j}=\sum_{k=1}^{n}\frac{1}{(2N_f)_k}=\sum_{k=1}^{n}\left(\frac{(\varepsilon_{a,j})_k}{\varepsilon_f'}\right)^{-\frac{1}{c}} \tag{7}$$

where $D_{s,j}$ is the damage index for the jth steel fiber, $(2N_f)_k$ is the number of half-cycles to failure at the strain amplitude $\varepsilon_{a,j}$ of the kth half-cycle, and n is the number of half-cycles in which $D_{s,j}$ is computed.

Strength degradation can be considered as a phenomenon that results from fatigue damage (Fig. 3) and is assumed to have a linear relationship with fatigue damage. The strength degradation is expressed as follows (Heo, 2009):

$$\lambda_{SR,j}=Z_d D_{s,j} \tag{8}$$

with $Z_d=\left(\dfrac{\varepsilon_f'}{C_d}\right)^{-\frac{1}{c}}$

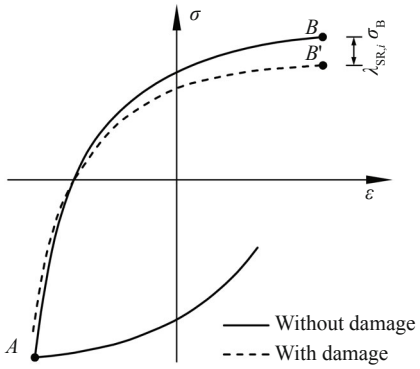

Fig. 3 Strength degradation

where $\lambda_{SR,j}$ is the strength degradation factor for the *j*th steel fiber and Z_d is the degradation constant.

In addition, suppose the stress-strain relationship of the former cycle is identical to that of the latter cycle after the first cycle. From this perspective, the strength degradation is an experimental phenomenon that results from a reduction in the effective cross-sectional area. Thus, according to Eq. (8), the effective area of a steel fiber is

$$\tilde{A}_{s,j}=(1-\lambda_{SR,j})\cdot e^{-\varepsilon_{p,j}}\cdot A_{s,j}=\left(1-\left(\frac{\varepsilon_f^{'}}{C_d}\right)^{-\frac{1}{c}}D_{s,j}\right)\cdot e^{-\varepsilon_{p,j}}\cdot A_{s,j} \tag{9}$$

and assuming that $\tilde{A}_{s,j}=0$ when $D_{s,j}=1$, where $\varepsilon_{p,j}$ is the plastic strain of the *j*th steel fiber, and $A_{s,j}$ is the cross-sectional area of the *j*th steel fiber without plastic deformation and fatigue damage.

For the sake of brevity and convenience, we set $D_{s,j}^{'}=1-\left(\frac{\varepsilon_f^{'}}{C_d}\right)^{-\frac{1}{c}}D_{s,j}\cdot e^{-\varepsilon_{p,j}}$, and Eq. (9) can be rewritten as

$$\tilde{A}_{s,j}=D_{s,j}^{'}\cdot A_{s,j} \tag{10}$$

According to existing literature (Dodd and Restrepo-Posada, 1995; Mansour *et al.*, 2001), the unloading stress-strain curve is essentially straight initially and then becomes curved. To reduce computational complexity and increase precision of the estimation of the unloading stress-strain curve, the unloading and reloading strain-stress curve between the unloading point and zero-stress point is approximated by a straight line with slope E_s, which is the initial tangent modulus of reinforcement (Hsu and Mo, 2010). Thus, the initial reloading modulus $\tilde{E}_{s,j}$ of the *j*th steel fiber is assumed to be a constant equal to $E_{s,j}$.

2.3 Damage at section level

The effective section stiffness $\tilde{\boldsymbol{K}}_{sec}(x)$, which has a relationship between the section resisting forces $\boldsymbol{F}_{sec}(x)$ and the corresponding deformations $\boldsymbol{d}_{sec}(x)$, can be determined by the assumption about the plane cross-section and principle of virtual displacements. In the uniaxial bending case, $\tilde{\boldsymbol{K}}_{sec}(x)$ takes the discrete form

$$\tilde{\boldsymbol{K}}_{sec}(x)=\begin{bmatrix}\sum_{i=1}^{n(x)}\tilde{E}_i\tilde{A}_i & -\sum_{i=1}^{n(x)}\tilde{E}_i\tilde{A}_i\cdot y_i\\ -\sum_{i=1}^{n(x)}\tilde{E}_i\tilde{A}_i\cdot y_i & \sum_{i=1}^{n(x)}\tilde{E}_i\tilde{A}_i\cdot y_i^2\end{bmatrix}=\begin{bmatrix}\sum_{i=1}^{n(x)}(1-D_i)\cdot E_iA_i & -\sum_{i=1}^{n(x)}(1-D_i)\cdot E_iA_i\cdot y_i\\ -\sum_{i=1}^{n(x)}(1-D_i)\cdot E_iA_i\cdot y_i & \sum_{i=1}^{n(x)}(1-D_i)\cdot E_iA_i\cdot y_i^2\end{bmatrix} \tag{11}$$

with $\boldsymbol{F}_{sec}(x)=\tilde{\boldsymbol{K}}_s(x)\cdot\boldsymbol{d}_s(x)$

$$\boldsymbol{F}_{sec}(x)=\left[N_x(x)\quad M_z(x)\right]^T$$

$$\boldsymbol{d}_{sec}(x)=\left[\varepsilon_x(x)\quad \varphi_z(x)\right]^T$$

where $n(x)$ is the total number of fibers in the section, $\tilde{E}_i$ is the initial reloading modulus of the *i*th fiber, $\tilde{A}_i$ is the effective area of the *i*th fiber, E_i is the initial tangent modulus of the *i*th fiber, A_i is the initial area of the *i*th fiber, D_i is the damage value for the *i*th fiber equal to $D_{c,i}$ or $D_{s,i}$, and y_i is the *y* coordinates of the *i*th fiber in the local-coordinate system (Fig. 4).

According to Eq. (11), the relationship between $\boldsymbol{K}_s(x)$ and $\boldsymbol{d}_s(x)$ can be expressed as

$$\begin{cases}N_x(x)=\left(\sum_{i=1}^{n(x)}(1-D_i)\cdot E_iA_i\right)\cdot\varepsilon_x(x)-\left(\sum_{i=1}^{n(x)}(1-D_i)\cdot E_iA_i\cdot y_i\right)\cdot\varphi_z(x) & (12a)\\ M_z(x)=-\left(\sum_{i=1}^{n(x)}(1-D_i)\cdot E_iA_i\cdot y_i\right)\cdot\varepsilon_x(x)+\left(\sum_{i=1}^{n(x)}(1-D_i)\cdot E_iA_i\cdot y_i^2\right)\cdot\varphi_z(x) & (12b)\end{cases}$$

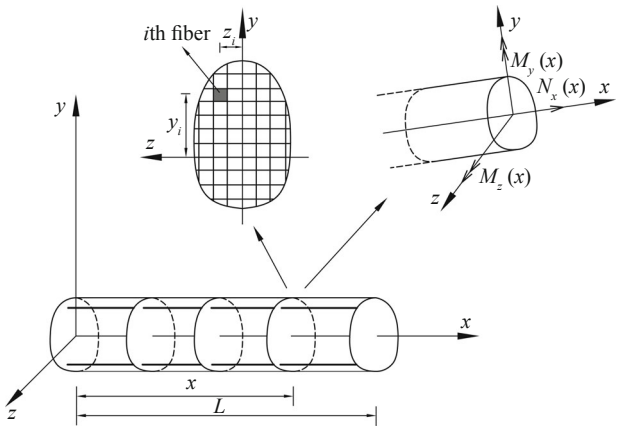

Fig. 4 Fiber beam-column element

By eliminating the contribution of $\varepsilon_x(x)$ to $M_z(x)$, Eq. (12b) can be rewritten as

$$M_z(x)+N_x(x)\cdot\overline{y}=\left[\sum_{i=1}^{n(x)}(1-D_i)\cdot E_iA_i\cdot y_i^2-\left(\sum_{i=1}^{n(x)}(1-D_i)\cdot E_iA_i\cdot y_i\right)^2\Big/\sum_{i=1}^{n(x)}(1-D_i)\cdot E_iA_i\right]\cdot\varphi_z(x) \quad (13)$$

with $\overline{y}=\left(\sum_{i=1}^{n(x)}(1-D_i)\cdot E_iA_i\cdot y_i\right)\Big/\sum_{i=1}^{n(x)}(1-D_i)\cdot E_iA_i$

Equation (13) adds a nonlinear correction term to the bending stiffness, which has a similar form as the equation proposed by Van Paepegem *et al.* (2005). Based on the bending stiffness degradation and according to Eq. (13), the damage index for the *k*th section $D_{\text{sec},k}$ can be defined as

$$D_{\text{sec},k}=1-\frac{\sum_{i=1}^{n(x)}(1-D_i)\cdot E_iA_i\cdot y_i^2-\left(\sum_{i=1}^{n(x)}(1-D_i)\cdot E_iA_i\cdot y_i\right)^2\Big/\sum_{i=1}^{n(x)}(1-D_i)\cdot E_iA_i}{\sum_{i=1}^{n(x)}E_iA_i\cdot y_i^2-\left(\sum_{i=1}^{n(x)}E_iA_i\cdot y_i\right)^2\Big/\sum_{i=1}^{n(x)}E_iA_i} \quad (14)$$

2.4 Damage at member level

To evaluate the damage to a member, the state of its component elements should be determined first. The effective element stiffness, which is used to estimate the damage to the element, can be obtained by the force-based method or displacement-based method (Li *et al.*, 2012).

In the force-based method, the effective element stiffness $\tilde{\boldsymbol{K}}_{\text{e}}(x)$, which is derived by inverting the effective element flexibility $\tilde{\boldsymbol{f}}_{\text{e}}(x)$, is expressed as

$$\tilde{\boldsymbol{K}}_{\text{e}}(x)=\tilde{\boldsymbol{f}}_{\text{e}}(x)^{-1}=\left[\int_L \boldsymbol{N}_{\text{f}}^{\text{T}}(x)\cdot\tilde{\boldsymbol{f}}_{\text{s}}(x)\cdot\boldsymbol{N}_{\text{f}}^{\text{T}}(x)\text{d}x\right]^{-1}=\left[\int_L \boldsymbol{N}_{\text{f}}^{\text{T}}(x)\cdot\tilde{\boldsymbol{K}}_{\text{s}}(x)^{-1}\cdot\boldsymbol{N}_{\text{f}}^{\text{T}}(x)\text{d}x\right]^{-1} \quad (15)$$

with $\boldsymbol{N}_{\text{f}}^{\text{T}}(x)=\begin{bmatrix}1 & 0 & 0 & 0 & 0\\ 0 & \frac{x}{L}-1 & \frac{x}{L} & 0 & 0\\ 0 & 0 & 0 & \frac{x}{L}-1 & \frac{x}{L}\end{bmatrix}$

Using the Gauss-Lobatto integration method (Welfert, 2010), the discrete form of Eq. (15) can be expressed by Eq. (16).

$$\begin{aligned}\tilde{\boldsymbol{K}}_{\text{e}}(x)=\tilde{\boldsymbol{f}}_{\text{e}}(x)^{-1}&=\Big\{L\Big[\omega_1\cdot\boldsymbol{N}_{\text{f}}^{\text{T}}(0)\cdot\tilde{\boldsymbol{f}}_{\text{s}}(0)\cdot\boldsymbol{N}_{\text{f}}^{\text{T}}(0)+\sum_{i=2}^{n-1}\omega_i\cdot\boldsymbol{N}_{\text{f}}^{\text{T}}(x_i)\cdot\tilde{\boldsymbol{f}}_{\text{s}}(x_i)\cdot\boldsymbol{N}_{\text{f}}^{\text{T}}(x_i)+\omega_n\cdot\boldsymbol{N}_{\text{f}}^{\text{T}}(L)\cdot\tilde{\boldsymbol{f}}_{\text{s}}(L)\cdot\boldsymbol{N}_{\text{f}}^{\text{T}}(L)\Big]\Big\}^{-1}\\&=\Big\{L\Big[\omega_1\cdot\boldsymbol{N}_{\text{f}}^{\text{T}}(0)\cdot\tilde{\boldsymbol{K}}_{\text{s}}(0)^{-1}\cdot\boldsymbol{N}_{\text{f}}^{\text{T}}(0)+\sum_{i=2}^{n-1}\omega_i\cdot\boldsymbol{N}_{\text{f}}^{\text{T}}(x_i)\cdot\tilde{\boldsymbol{K}}_{\text{s}}(x_i)^{-1}\cdot\boldsymbol{N}_{\text{f}}^{\text{T}}(x_i)+\omega_n\cdot\boldsymbol{N}_{\text{f}}^{\text{T}}(L)\cdot\tilde{\boldsymbol{K}}_{\text{s}}(L)^{-1}\cdot\boldsymbol{N}_{\text{f}}^{\text{T}}(L)\Big]\Big\}^{-1}\end{aligned} \quad (16)$$

where L is the length of the member, and ω_i and x_i are the quadrature weight and location of the *i*th section.

If an individual member is simulated by one element, the relationship between the rod-end forces and the rod-end deformations in rigid-body mode can be directly described by the coordination-transformed form of Eq. (16). If an individual member is discretized into several elements, the effective member stiffness matrix in rigid-body mode can be obtained by assembling all of the effective element stiffness matrices, and then static condensation is applied to the stiffness matrix to remove the degrees of freedom associated with internal nodes. In both cases (Fig. 5), the relationship between the rod-end forces $\boldsymbol{F}_{\text{memeber}}$ and the rod-end deformations $\boldsymbol{d}_{\text{memeber}}$ for the member is expressed as

$$\boldsymbol{F}_{\text{member}}=\tilde{\boldsymbol{K}}_{\text{member}}\cdot\boldsymbol{d}_{\text{member}} \quad (17)$$

namely

$$\begin{Bmatrix}F_{\text{px}}\\F_{\text{py}}\\M_{\text{p}}\\F_{\text{qx}}\\F_{\text{qy}}\\M_{\text{q}}\end{Bmatrix}=\begin{bmatrix}\tilde{k}_{u_{\text{p}},u_{\text{p}}} & \tilde{k}_{1,2} & \tilde{k}_{1,3} & \tilde{k}_{1,4} & \tilde{k}_{1,5} & \tilde{k}_{1,6}\\ \tilde{k}_{2,1} & \tilde{k}_{v_{\text{p}},v_{\text{p}}} & \tilde{k}_{2,3} & \tilde{k}_{2,4} & \tilde{k}_{2,5} & \tilde{k}_{2,6}\\ \tilde{k}_{3,1} & \tilde{k}_{3,2} & \tilde{k}_{\phi_{\text{p}},\phi_{\text{p}}} & \tilde{k}_{3,4} & \tilde{k}_{3,5} & \tilde{k}_{3,6}\\ \tilde{k}_{4,1} & \tilde{k}_{4,2} & \tilde{k}_{4,3} & \tilde{k}_{u_{\text{q}},u_{\text{q}}} & \tilde{k}_{4,5} & \tilde{k}_{4,6}\\ \tilde{k}_{5,1} & \tilde{k}_{5,2} & \tilde{k}_{5,3} & \tilde{k}_{5,4} & \tilde{k}_{v_{\text{q}},v_{\text{q}}} & \tilde{k}_{5,6}\\ \tilde{k}_{6,1} & \tilde{k}_{6,2} & \tilde{k}_{6,3} & \tilde{k}_{6,4} & \tilde{k}_{v_2,v_2} & \tilde{k}_{\phi_{\text{q}},\phi_{\text{q}}}\end{bmatrix}\begin{Bmatrix}u_{\text{p}}\\v_{\text{p}}\\\phi_{\text{p}}\\u_{\text{q}}\\v_{\text{q}}\\\phi_{\text{q}}\end{Bmatrix} \quad (18)$$

where $\tilde{\boldsymbol{K}}_{\text{member}}$ is the effective member stiffness that has been condensed, F_{px}, u_{p} and $\tilde{k}_{u_{\text{p}},u_{\text{p}}}$ are the force, displacement and effective rod-end stiffness in the X direction at Node p, F_{py}, v_{p} and $\tilde{k}_{v_{\text{p}},v_{\text{p}}}$ are the force, displacement and effective rod-end stiffness in the Y direction at Node p, M_{py}, ϕ_{p} and $\tilde{k}_{\phi_{\text{p}},\phi_{\text{p}}}$ are the bending moment, rotation and effective rod-end bending stiffness at Node p, F_{qx}, u_{q} and $\tilde{k}_{u_{\text{q}},u_{\text{q}}}$ are the force, displacement and effective rod-end stiffness in the X direction at Node q, F_{qY}, v_{q} and $\tilde{k}_{v_{\text{q}},v_{\text{q}}}$ are the force, displacement and effective rod-end stiffness in the Y direction at Node q, M_{q}, ϕ_{q} and $\tilde{k}_{\phi_{\text{q}},\phi_{\text{q}}}$ are the bending moment, rotation and effective rod-end bending stiffness at Node q, and the left elements of $\tilde{\boldsymbol{K}}_{\text{member}}$ are the effective stiffness influence coefficients.

The damage to the member D_{memeber} can be described by the effective rod-end bending stiffness as

Fig. 5 Beam element with nodal displacements and forces

$$D_{\text{member}} = \max\left(1-\frac{\tilde{k}_{\phi_p,\phi_p}}{\tilde{k}_{\phi_p,\phi_p}}, 1-\frac{\tilde{k}_{\phi_q,\phi_q}}{\tilde{k}_{\phi_q,\phi_q}}\right) \tag{19}$$

where k_{ϕ_p,ϕ_p} and k_{ϕ_q,ϕ_q} are the initial rod-end bending stiffness corresponding to $\tilde{k}_{\phi_p,\phi_p}$ and $\tilde{k}_{\phi_q,\phi_q}$.

2.5 Damage at story and structure level

The effective stiffness matrix of a given story (Fig. 6(a)) can be determined by assembling the effective member stiffness matrices, which have been obtained and condensed using the direct stiffness method according to node numbers. The effective lateral stiffness for the equivalent story $\tilde{\boldsymbol{K}}_{\text{story}}$ (Fig. 6(b)), which relates the story shear $\boldsymbol{F}_{\text{story}}$ to the story deformation $\boldsymbol{d}_{\text{story}}$(Chopra, 1995), is obtained by neglecting the axial deformations of beams and condensing out all of the degrees of freedoms except that are associated with the horizontal displacements and is expressed as

$$\boldsymbol{F}_{\text{story}} = \tilde{\boldsymbol{K}}_{\text{story}} \cdot \boldsymbol{d}_{\text{story}} \tag{20}$$

namely

$$\begin{Bmatrix} f_s \\ f_{s-1} \end{Bmatrix} = \begin{bmatrix} \tilde{k}_{u_s,u_s} & \tilde{k}_{u_s,u_{s-1}} \\ \tilde{k}_{u_{s-1},u_s} & \tilde{k}_{u_{s-1},u_{s-1}} \end{bmatrix} \begin{Bmatrix} u_s \\ u_{s-1} \end{Bmatrix} \tag{21}$$

where f_s, u_s and $\tilde{k}_{u_s,u_s}$ are the shear, displacement and effective lateral stiffness in the X direction at node s, f_{s-1}, u_{s-1} and $\tilde{k}_{u_{s-1},u_{s-1}}$ are the shear, displacement and effective lateral stiffness in the X direction at node s-1, and $\tilde{k}_{u_s,u_{s-1}}$ and $\tilde{k}_{u_{s-1},u_s}$ are the effective stiffness influence coefficients.

The damage to the story D_{story} can be described by its effective lateral stiffness as

$$D_{\text{story}} = \max\left(1-\frac{\tilde{k}_{u_s,u_s}}{k_{u_s,u_s}}, 1-\frac{\tilde{k}_{u_{s-1},u_{s-1}}}{k_{u_{s-1},u_{s-1}}}\right) \tag{22}$$

where k_{u_s,u_s} and $k_{u_{s-1},u_{s-1}}$ are the initial story lateral stiffness corresponding to $\tilde{k}_{u_s,u_s}$ and $\tilde{k}_{u_{s-1},u_{s-1}}$.

After obtaining all of the effective stiffness matrices of the equivalent stories that have been condensed (Fig. 7(a)), the effective stiffness matrix of a structure (Fig. 7(b)) can be determined by the direct stiffness method according to the serial number of a story. The effective lateral stiffness for the equivalent structure $\tilde{\boldsymbol{K}}_{\text{structure}}$ (Fig. 7(c)), which relates the structure shears $\boldsymbol{F}_{\text{structure}}$ to the structure deformations $\boldsymbol{d}_{\text{structure}}$, is obtained by condensing out the degrees of freedom associated with internal nodes and expressed as

$$\boldsymbol{F}_{\text{structure}} = \tilde{\boldsymbol{K}}_{\text{structure}} \cdot \boldsymbol{d}_{\text{structure}} \tag{23}$$

namely

$$\begin{Bmatrix} F_0 \\ F_n \end{Bmatrix} = \begin{bmatrix} \tilde{k}_{u_0,u_0} & \tilde{k}_{u_0,u_n} \\ \tilde{k}_{u_n,u_0} & \tilde{k}_{u_n,u_n} \end{bmatrix} \begin{Bmatrix} u_0 \\ u_n \end{Bmatrix} \tag{24}$$

where F_0, u_0 and $\tilde{k}_{u_0,u_0}$ are the force, displacement and effective lateral stiffness in the X direction at node 0, and F_n, u_n and $\tilde{k}_{u_n,u_n}$ are the force, displacement and effective lateral stiffness in the X direction at node n.

Given that the influence of damage location, such as to a lower story, is more critical than that to an upper story, the structure damage $D_{\text{structure}}$ can be described by its effective lateral stiffness at top node n and expressed as

$$D_{\text{structure}} = 1-\frac{\tilde{k}_n}{k_n} \tag{25}$$

where k_n is the initial structure's lateral stiffness corresponding to $\tilde{k}_n$.

3 Validation of the damage model in RC columns

In this section, several columns were selected to verify the established damage model at fiber, section and member levels. First, the damage analysis results and numerical simulation results of two RC columns with different reinforcement rates were compared. Then, an RC column was selected to compare the damage analysis results with the experimental results. Finally, examples of application of the established damage model to a column subjected to seismic actions were presented. In the following numerical models, the simplified Chang and Mander concrete model was adopted for the confined concrete and unconfined concrete, and the modified reinforcing steel model was adopted for the reinforcing steel bars.

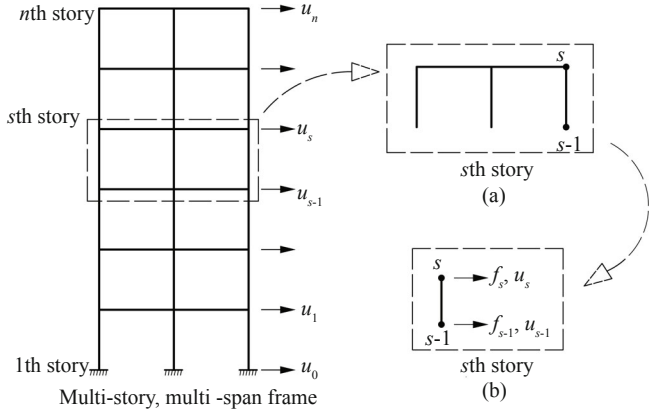

Fig. 6 Damage analysis at story level

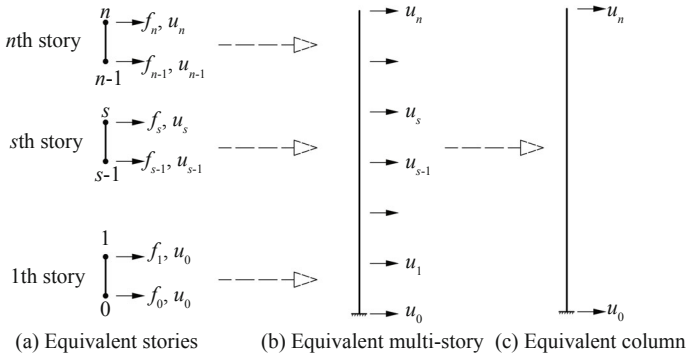

Fig. 7 Damage analysis at structure level

3.1 Numerical validation of the damage model

Two columns with different reinforcement ratios tested by Saatcioglu and Grira (1999) were chosen as an example to illustrate and verify the damage model developed. The cross-sections of the columns, denoted as BG-2 and BG-5, were square-shaped with dimensions of 350 mm × 350 mm. The geometry of the column specimens is shown in Fig. 8; all of the longitudinal reinforcing bars had a diameter of 19.5 mm, and the transverse reinforcements had diameters of 9.5 mm and a pitch of 76 mm apart centered throughout the length of the columns. The longitudinal reinforcing bars had a yield stress of 455.6 MPa and an ultimate tensile strength of 660 MPa. The two columns were subjected to approximately 40 percent of their nominal axial load strength, and lateral deformation reversals were applied horizontally at a point 1645 mm above the column footing.

Figure 9 shows the numerical model build-up and fiber element discretization for the RC columns. Each column in the numerical model consists of five elements, and each reinforcing steel bar is treated as a single fiber. The element lengths are identical, and there are three integration points for each element. The mechanical parameters for the concrete are shown in Table 1.

The lateral load-lateral displacement curves for the two column specimens are shown in Figs. 10 and 11. The figures show good agreement between the simulation results and the experimental results, where the stiffness degradation of the columns under cycle loadings is rationally reflected. This result confirms that the developed fiber analytical model can be used to estimate the damage to the selected column specimens.

The damage evolution process of each concrete fiber and steel fiber can be obtained using the proposed damage model at the fiber level. Cross-section N1', which is located between Points 1 and 2 of column BG-5 (Fig. 9), was chosen to account for the evolution process. The compressive damage to Concrete Fibers C1, C2 and C3 is shown in Fig. 12, and the fatigue damage to steel S1 and S2 is shown in Fig. 13. As expected, the computed damage index value of cover Concrete Fiber C1 reached 1 considerably earlier than those of C2 and C3, and the damage index value of Steel Fiber S1 is considerably greater than that of S2 because of their positions. For Concrete Fibers C2 and C4, which have opposite local y values, the damage index value of C2 is smaller than that of C4 before the former reaches 1 due to the effect of lateral confinement (Fig. 14).

Sections N1, N2, N3 and N6 (Fig. 9) were chosen to account for the damage evolution process of column sections. The comparison in Fig. 15 shows that the closer to the column footing, the faster the evolution

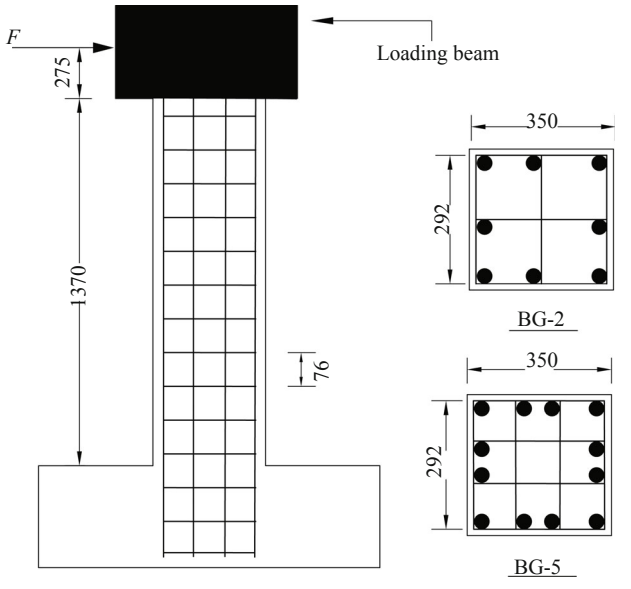

Fig. 8 Geometry of the column specimens (Saatcioglu and Grira, 1999)

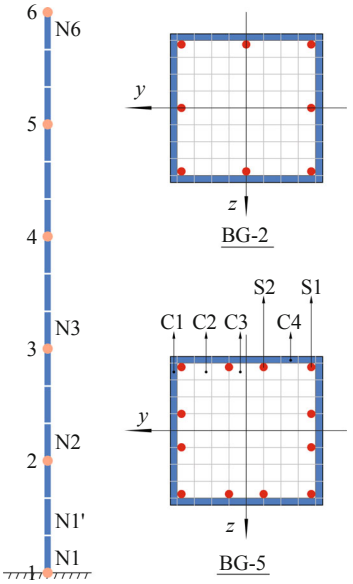

Fig. 9 Discretization of the column and cross section

Table 1 Parameters for the confined and unconfined concrete models

Column tag	Concrete type	Cylinder compressive strength (MPa)	Strain at cylinder compressive stress (10^{-3})	Initial elastic modulus (10^4 MPa)	Tensile strength (MPa)	Strain at peak tensile stress (10^{-4})
BG-2	Confined concrete	52.8	5.816	3.04	3.56	2.341
	Unconfined concrete	33.0	2.079	3.04	3.56	2.341
BG-5	Confined concrete	60.0	7.179	3.04	3.56	2.341
	Unconfined concrete	33.0	2.079	3.04	3.56	2.341

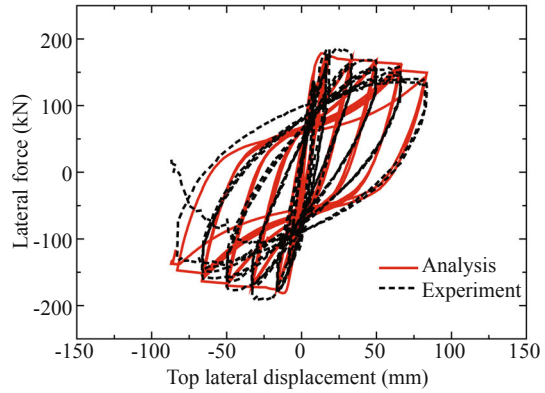

Fig. 10 Lateral load–lateral displacement relationship for Specimen BG-2

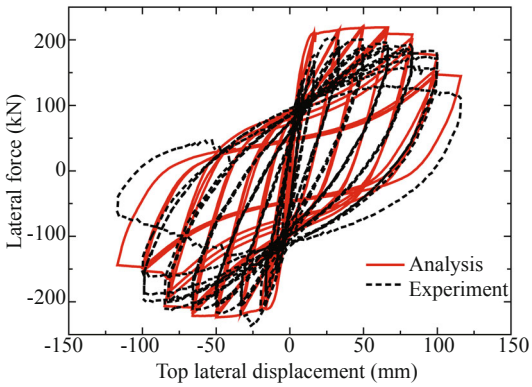

Fig. 11 Lateral load–lateral displacement relationship for Specimen BG-5

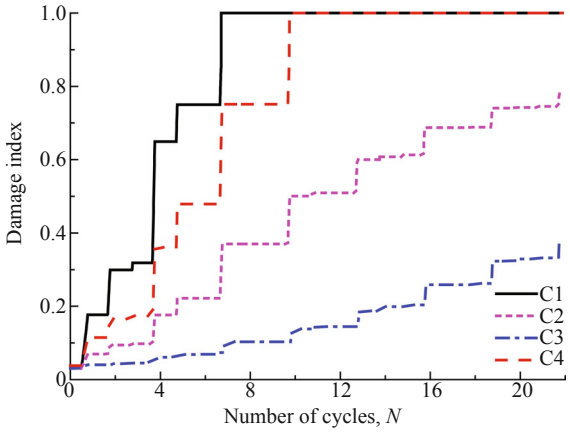

Fig. 12 Compression damage evolutions of the concrete fibers

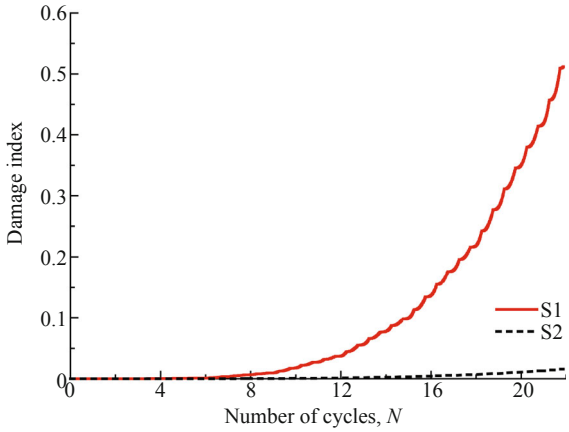

Fig. 13 Damage evolutions of the steel fibers

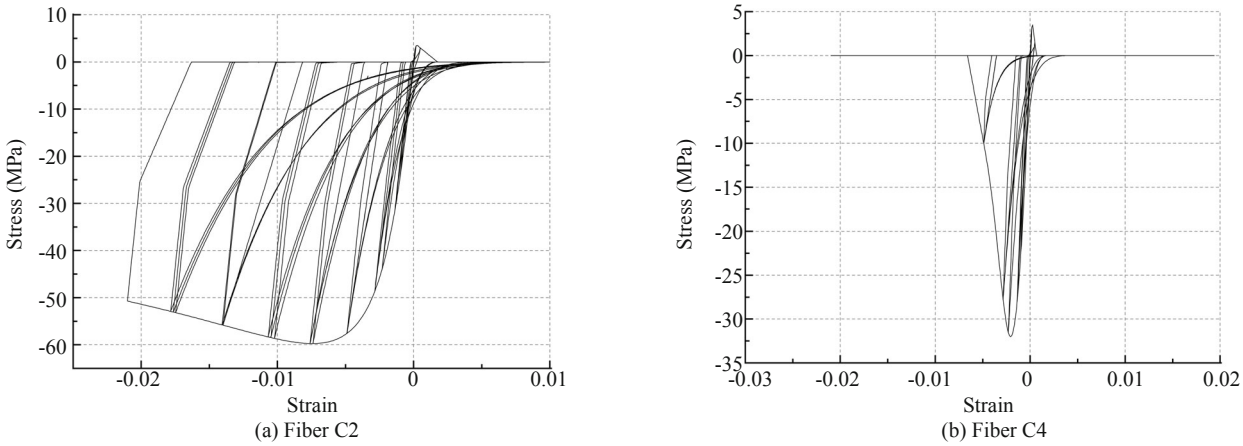

Fig. 14 Stress-strain response of Fiber C2 and Fiber C4

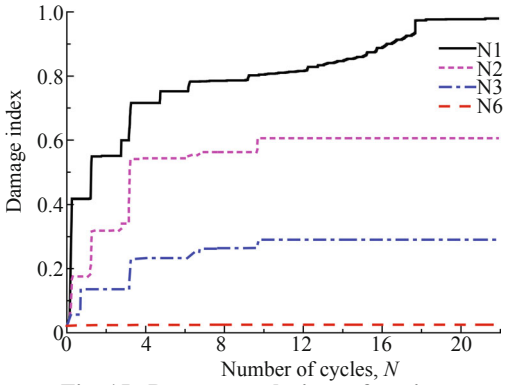

Fig. 15 Damage evolutions of sections

of damage to the section chosen will be. The damage index of Section N1 approached 0.9795 at the end of the reversed cyclic loading, whereas the damage index of Section N6 remained very small (0.0250). These results are in excellent agreement with the analysis results (Fig. 16).

The damage evolutions of Columns BG-2 and BG-5 are shown in Fig. 17. As the longitudinal reinforcement ratio of BG-5 (2.94%) is higher than that of BG-2 (1.96%), the damage index value of BG-5 is smaller than that of BG-2 at the end of the loading process, and BG-5 exhibited better displacement ductility. Additionally, the damage indices of both columns were almost equal and

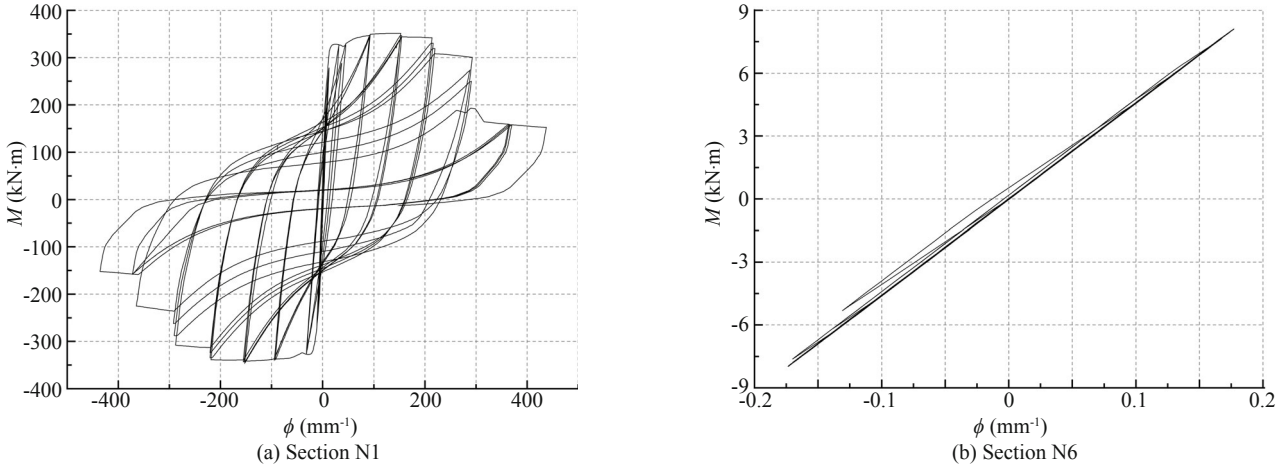

Fig. 16 Moment-curvature response of Section N1 and Section N6

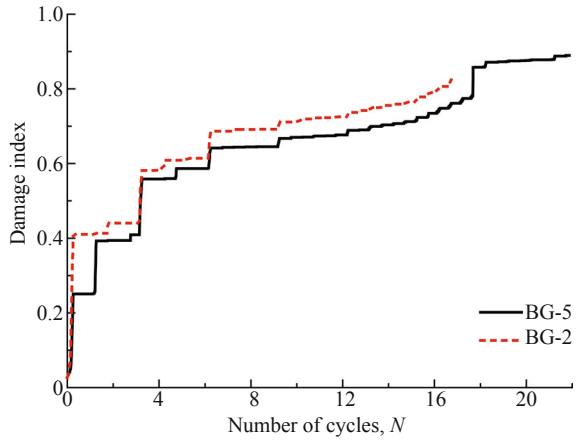

Fig. 17 Damage evolution in Columns BG-2 and BG-5

increased rapidly for the top lateral displacement of less than 20 mm, possibly because the stiffness degradation in a column primarily results from the development of cracks at the early stage of loading.

3.2 Experimental validation of the damage model

To verify the damage model developed at the section and member levels, an RC column tested in Tsinghua University was selected to compare the damage analysis results with the experimental results. The specimen is chosen from the work of Lu *et al*. (2012a, b) and Xie *et al*. (2015), where it is referred to as Middle Column C. The geometry of the column specimen is shown in Fig. 18. In the test, a constant vertical load of 256.25 KN was first applied on the top of the column, and then cyclically reversed lateral loading was applied at a point 750 mm from the column footing.

The column specimen is modeled with five displacement-based elements, and each element is integrated with three Gauss-Lobatto points. All elements have the same length, and each transversal section has been discretized into 10×10 fibers. The mechanical parameters for the concrete and reinforcing bars are listed in Table 2 and Table 4(a), respectively. The lateral load-lateral displacement response for the column is shown in Fig. 19. The analytical results exhibit rational correspondence with the experimental results.

Five displacement points, A, B, C, D, and E, were selected on the load-displacement curve (Fig. 20), and their displacements are 1.134 mm, 6.885 mm, 17.408 mm, 37.683 mm and -2.649 mm, respectively. Fig. 21(a) shows the failure process of the column, and Fig. 21(b) shows the corresponding section damage of the column. The dimension of the squares marked on the specimen surface was about 50 mm × 50 mm (Fig. 21(a)). When the lateral displacement reached 0.429 mm (Point A), no obvious cracks were observed. Though the tensile strain in the concrete located on both sides of the column base may be smaller than the ultimate tensile strain, the tensile stresses are not proportional to tensile strains which leading to the small section damage in the column base (Fig. 21(a)). Meanwhile, the damage index of the column approached 0.1444. Initial cracks were observed on the left side of the specimen at a lateral displacement of 3.016 mm (Point B), and one of the horizontal cracks propagated to a point near the neutral plane. At this stage, the section damage increased significantly, and the damage index of the column approached 0.5828. Cracking of the right side was observed in the very next cycle in

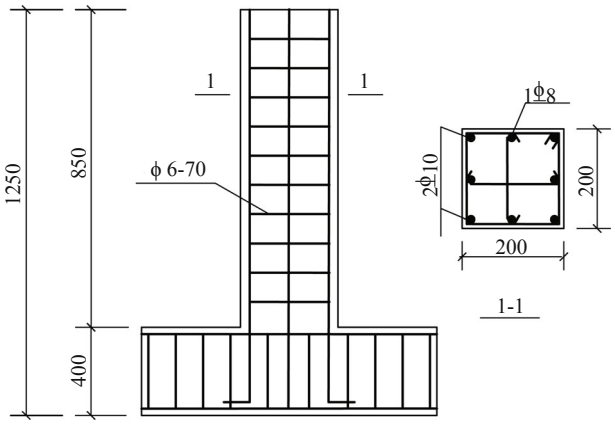

Fig. 18 Geometry of the column specimen (Lu *et al*., 2012; Xie *et al*., 2015)

Table 2 Parameters for the confined and unconfined concrete

Concrete type	Cylinder compressive strength (MPa)	Strain at cylinder compressive stress (10^{-3})	Initial elastic modulus (10^4 MPa)	Tensile strength (MPa)	Strain at peak tensile stress (10^{-4})
Confined concrete	30.8	2.591	2.69	3.02	2.247
Unconfiend concrete	23.8	1.916	2.69	3.02	2.247

Table 3 Features of three ground motions

Earthquake name	Station name	Closest distance to rupture plane (km)	PGA (g)	PGV (cm/s)	PGD (cm)
Imperial Valley	El Centro Array #9	6.09	0.2584	31.74	18.01
Loma Prieta	LGPC	3.88	0.7835	77.15	42.67
Kern County	Taft Lincoln School	38.89	0.1728	15.72	9.34

Table 4 Mechanical properties of materials

(a) Steel bar

Mechanical property	ϕ4	ϕ6	ϕ8	ϕ10
Yield strength f_y (MPa)	390	441	582	481
Yield strain	0. 0021	0. 0022	0. 0020	0. 0020
Ultimate strength f_u (MPa)	414	529	855	745
Modulus of elasticity E_s (MPa)	195000	203941	289850	265433
Elongation factor (%)	26.7	34.2	28.8	23.6

(b) Concrete

Story	Concrete type	Member tag	Section type	Cylinder compressive strength (MPa)	Strain at the peak compressive stress (10^{-3})	Initial Elastic modulus (10^4MPa)
1	Confined	Column11, Column12, Column13, Column14	Densified	32.2	2.558	2.75
			Undensified	28.7	2.279	2.75
		Beam11, Beam12, Beam13	Densified	27.7	2.202	2.75
			Undensified	26.4	2.101	2.75
	Unconfined			25.2	1.943	2.75
2	Confined	Column21, Column24	Densified	27.8	2.308	2.71
			Undensified	26.0	2.154	2.71
		Column22, Column23	Densified	31.2	2.584	2.71
			Undensified	27.6	2.292	2.71
		Beam21, Beam22, Beam23	Densified	26.7	2.211	2.71
			Undensified	25.4	2.105	2.71
	Unconfined			24.1	1.923	2.71
3	Confined	Column31, Column34	Densified	27.1	2.319	2.67
			Undensified	25.2	2.159	2.67
		Column32, Column33	Densified	30.4	2.603	2.67
			Undensified	26.9	2.301	2.67
		Beam31, Beam32, Beam33	Densified	25.9	2.218	2.67
			Undensified	24.6	2.109	2.67
	Unconfined			23.4	19.71	2.67

the reverse direction of loading. After two cycles, no new cracks occurred and the width of the existing cracks grew steadily. At Point C, the damage index value of the column was 0.6908, and the corresponding experimental phenomena and section damage are shown in Fig. 21. As the lateral loading continued to increase, cover concrete started to spall off. At Point D, all of the cover concrete at the column base completely crushed, and section damage was caused mainly by the compressive damage of concrete fibers rather than their tensile damage. At the end of the loading (Point E), the carrying capacity of the column was approached, and the concrete at the base exhibited severe damage. The comparison between the experimental results and section damage of the column indicates that the established damage model shows a reasonable correspondence with the experimental phenomena at the section level.

From Fig. 21(b), it is observed that the damage of the

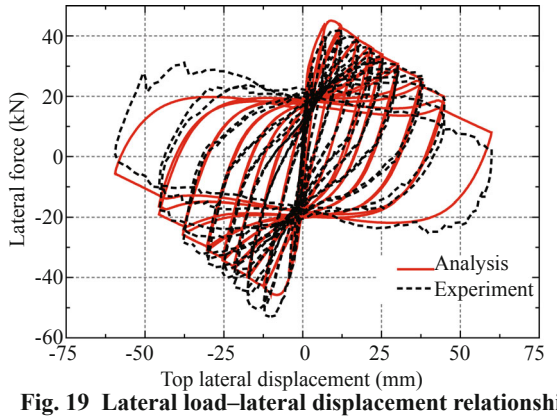

Fig. 19 Lateral load–lateral displacement relationship

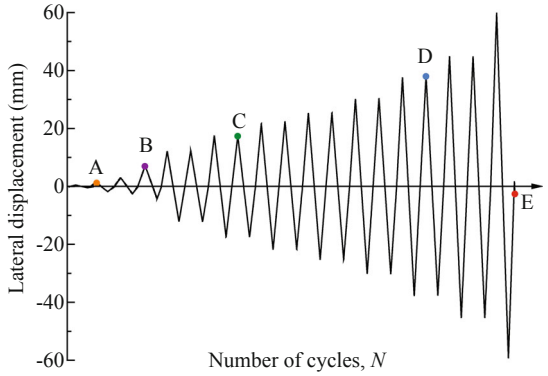

Fig. 20 Top displacement history

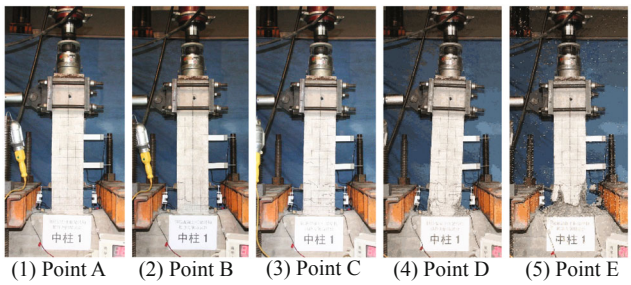

(a) Experimental results of the column during the test

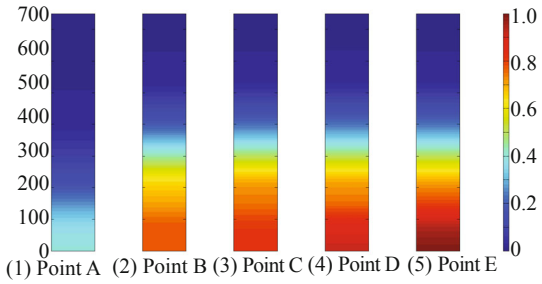

(b) Damage contour maps of the column

Fig. 21 Damage progression of the column

selected sections was higher for sections that were closer to the column footing at the same lateral displacement. Furthermore, the results also indicate the section damage progressed rapidly from the base up to a distance of 200 mm, while the section damage in the remaining area progressed slowly during the loading process, which is consistent with the experiment (Fig. 21(a)). Thus, the established damage model can accurately identify the location and magnitude of the local damage in real time.

Figure 22 compares the proposed damage model with the modified softening index (Kunnath *et al.*, 1997)) and Park-Ang model (Park and Ang, 1985). The damage index proposed in this study and modified softening index increase rapidly in the early stage of testing and slowly from this point to failure, which well reflects the tensile and compressive damage to concrete. The Park-Ang model shows a gradual progression throughout the loading history. All of the three damage models can adequately show the final damage.

3.3 Numerical validation of the damage model under seismic actions

To further verify the damage model, the specimen selected in Section 3.2 was considered under seismic actions. The same fiber element model as Section 3.2 was employed and the vertical load acting on the column was also the same. A 14 t-lumped mass is located at the top of the column. The Imperial Valley, Loma Prieta and Taft records (Table 3) have been selected for the following nonlinear time history analysis. PGA values for the input ground motions started from 0.0g and gradually increased to 0.4g with the increasing step of 0.05g. Figure 23 shows that column damage indices constantly increased as the PGA values increased, and Imperial Valley motion could cause more serious damage under the same PGA value.

To illustrate the influence of the number of elements on the established damage model, the column also has been modeled with a single displacement-based element which has five Gauss-Lobatto integration points. Figure 24 shows a comparison of the damage curves between two different numbers of elements. The curves show that no major differences between two elements are recognizable, while one element with five Gauss-Lobatto points is sufficient for accurate integration with the displacement-based element quantities. Therefore, throughout the following analysis, a single displacement-based element with a constant number of Gauss-Lobatto integration points per column equal to five will be used.

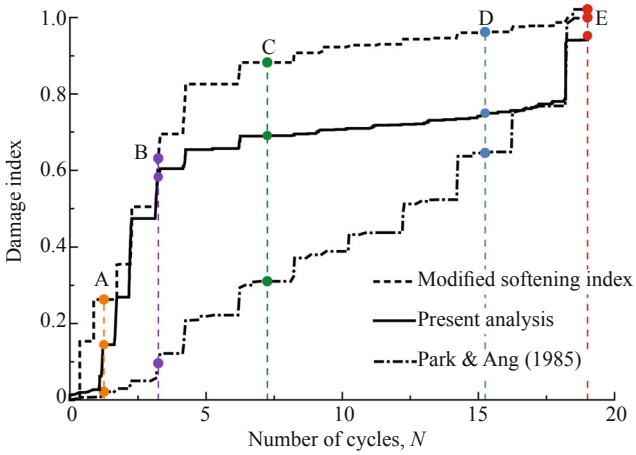

Fig. 22 Damage evolution of the column

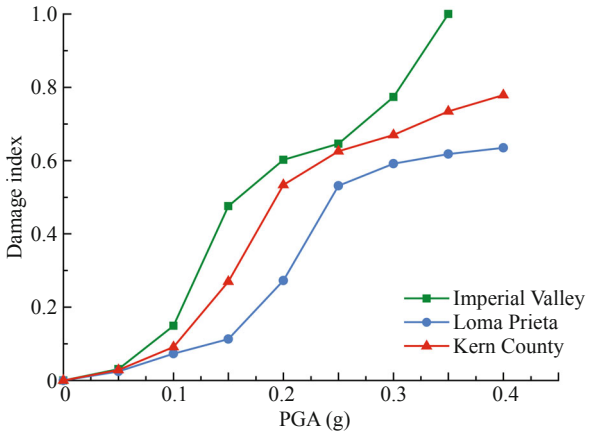

Fig. 23 Damage curve of the column under earthquake with various intensity

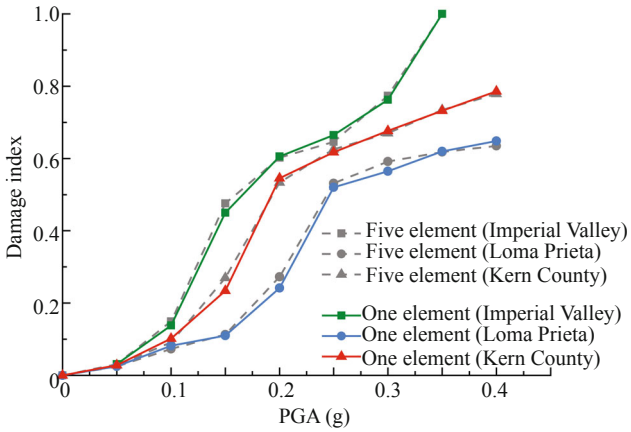

Fig. 24 Damage curve of the column using different number of elements under earthquake with various intensity

4 Validation of the damage index in a RC frame

To verify the established damage model at the member, story and structure levels, one three-story three-span reinforced concrete plane frame tested by Lu *et al.* (2012a, b) and Xie *et al.* (2015) in Tsinghua University was chosen for the study. The frame was at 1:2 scale, and its details are depicted in Fig. 25.

Figure 25 also shows the tags of nodes, beams and columns. Each beam and column in the numerical model consists of one displacement-based element, and each column and beam element has five and six Gauss-Lobatto integration points, respectively. For the reinforcing bars, the modified reinforcing steel model has been adopted, and the mechanical parameters in engineering coordinates are listed in Table 4(a). For the concrete, the simplified Chang and Mander concrete model has been used, and compressive mechanical parameters for the concrete are listed in Table 4(b). Tensile strengths of 3.11 MPa, 3.05 MPa and 3.00 MPa are assumed respectively for the concrete of the first, second and third story, while tensile strains of 2.263×10^{-4}, 2.251×10^{-4} and 2.242×10^{-4} are assumed respectively for the concrete of the first, second and third story.

Examples of validation and application of the damage model to nonlinear analysis of the selected reinforced concrete frame are presented in this section, including tests using cyclic loads and subjected to seismic actions.

4.1 Reinforced concrete frame subjected to cyclic loads

In the example, constant vertical loads were first applied to the top of the columns, and then horizontal loads were applied to the frame at floor level. The horizontal loads were controlled by the force-displacement mixed method and the force ratios among the third, second, and first stories was 18:2:1. The reversed cyclic loads followed the aforementioned loading pattern with an incremental amplitude, with each amplitude in the

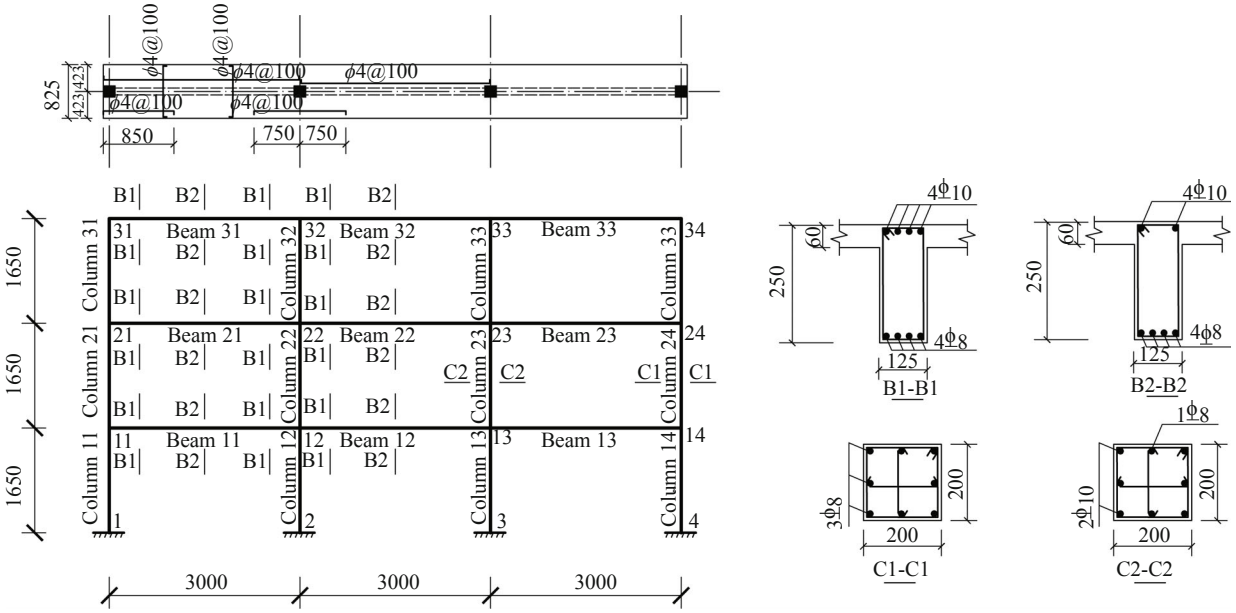

Fig. 25 Geometry and sections of the frame

loading history repeated twice. The analytical and experimental base shear-top displacement response of the frame is shown in Fig. 26 and the analytical results exhibited good agreement with the experimental results.

For conciseness and clarity, Fig. 27 only shows the damage evolution process of three columns in the first story. It can be observed that the final damage index values of Column12, Column13 and Column14 were 0.7992, 0.8630 and 0.7430, respectively. The analysis results have the same variation trend as the experiment results where the damage to Column13, Column12, and Column14 decreased in turn at the end of the loading.

Eight displacement points were selected on the top displacement curve as shown in Fig. 28, and their displacements were 8.05 mm, 33.27 mm, 51.58 mm, 83.66 mm, 101.55 mm, 139.24 mm, 164.42 mm and 189.98 mm, respectively. Analyzing the damage evolution process of each story (Fig. 29), it is observed that all of the story damage values were small (Point A) at the early stages of the loading. As the lateral displacement increased, diagonal cracks appeared at the middle joints of the first story (Point B), while the damage indices of the first story and second story were 0.40949 and 0.46809, respectively. Then, concrete crushing was obvious at the bottom of the side and middle columns, and concrete peeling took place at the joints (Point D). The damage index of the first story was 0.70983. Afterward, severe concrete spalling was observed on the cover layer at the bottom of Column13 (Point F), while the damage index of the first story reached 0.75862. Finally, concrete at the bottom of Column13 completely crushed, and the damage value of Column 13 was 0.8630. During this process, the damage values of the first story were higher than those of the other two stories under the same displacement (Point B → Point G). The result is confirmed by experiment where the frame failed mainly because of the damage to the first story (Fig. 30).

By comparing the story damage indices (Fig. 31) and the inter-story drifts (Fig. 32), it can be seen that their values increased with an increase in displacement, showing rational correspondence with each other except at three displacement points (Points C, D and E). At Points C, D and E, the inter-story drifts of the first story (0.01008, 0.01757, 0.02236) were smaller than those of the second story (0.01255, 0.02041, 0.02464), but the story damage indices of the first story (0.62656, 0.70983 and 0.72346) were greater than those of the second story (0.59216, 0.65515, 0.66712). This occurred since the concrete compression strength of the first story was higher than that of the second story (Fig. 25 and Table 4(b)). Equation (5) indicates that the higher the compression strength a concrete fiber has, the faster the stiffness degradation and the more serious damage it will suffer under the same strain. Given the relationship between strain and inter-story drift, stories with different

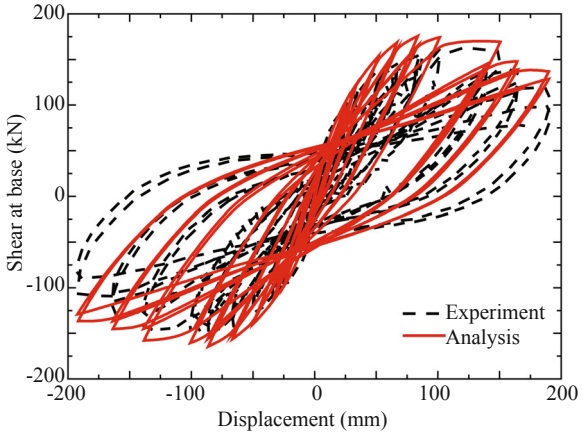

Fig. 26 Base shear–top displacement

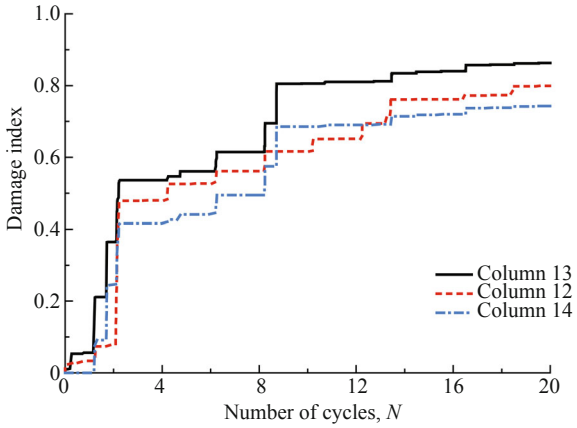

Fig. 27 Damage evolutions in column 12, column 13 and column 14

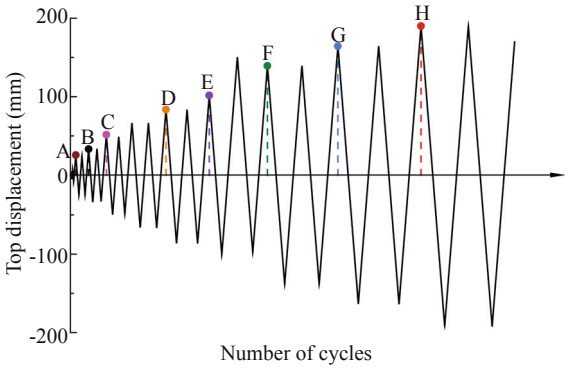

Fig. 28 Top displacement history

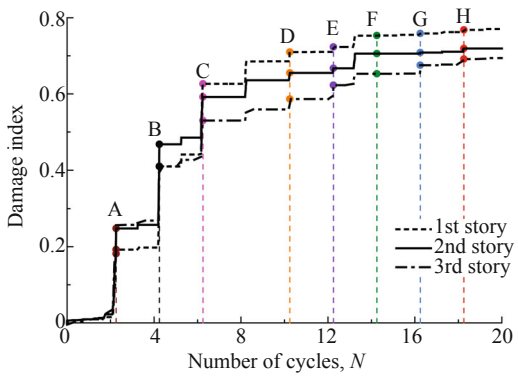

Fig. 29 Damage evolutions in each story

(a) Global failure (b) Failure of column

Fig. 30 Failure mode of RC frame (Lu *et al*., 2012)

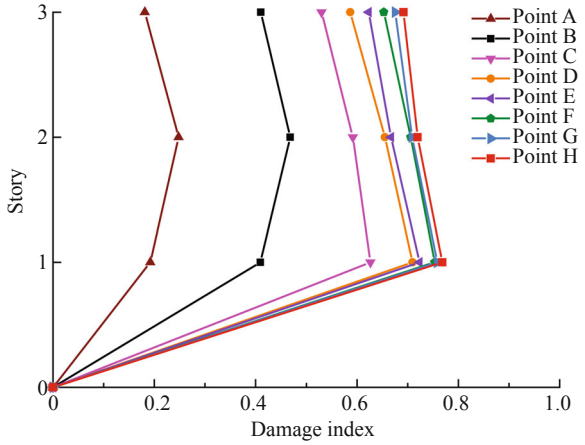

Fig. 31 Damage evolutions in each story at the specified displacement

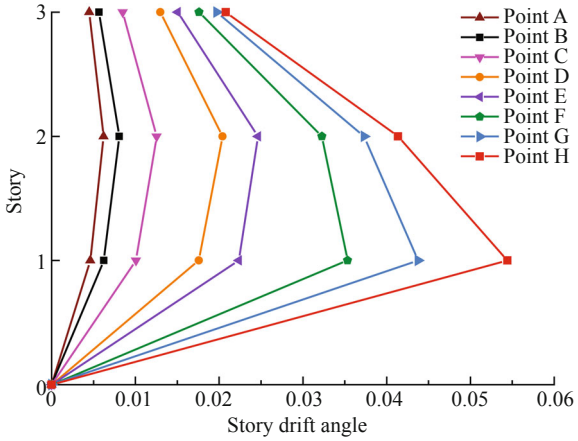

Fig. 32 Inter-story drift at the specified displacement

stiffnesses may have different damage values even though they may have the same inter-story drifts. That's also why different drift limitation values have been suggested for different structural systems.

A comparison of the damage evolution process of the frame and stories is presented in Fig. 33. The comparison illustrates that the damage index values of the frame belonged to the interval which was determined by the damage index values of the stories. The result indicates that story damage can be accurately transformed into structure damage by the proposed damage model accurately without introducing weighting coefficients.

4.2 Reinforced concrete frame subjected to seismic acceleration

This example studies the evolutions of the damage in the three-story three-span RC plane frame of Fig. 25 subjected to horizontal ground motion. The same finite element model as in Section 4.1 was employed and the vertical loads acting on the frame were the same as before. The masses are lumped at the beam-to-column intersections. The values of the computed masses were 6.00 t for the side beam-to-column intersections, while 11.83 tons were utilized for the middle beam-to-column intersections. In the present study, 'Rayleigh damping', which is a linear combination of the mass and stiffness matrices, was used.

The far-field earthquake Imperial Valley (1945) was used for the nonlinear dynamic analysis, and PGA values for the input load started from 0.06g and gradually increased to 0.42g PGA. Figure 34 shows the evolution of the story and global damage indices. As expected, story and global damage indices constantly

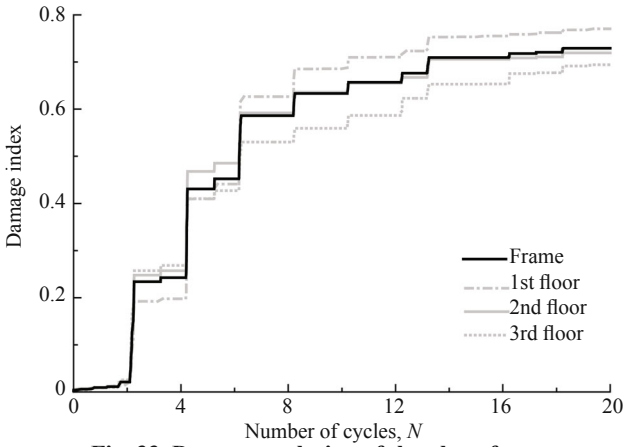

Fig. 33 Damage evolution of the plane frame

increased in time, and possessed a larger value as the PGA values increased. Comparing the damage indices of each story (Fig. 34(a), (b), (c)), it can be observed that the damage indices of the first, second and third story decreased successively under the same PGA value at the same time. Damage also decreased with the height.

5 Conclusions

To identify the damage states of an RC member and structure accurately in real time, and to establish a close link between damage indices at various levels, a damage model for RC members and frames was established based on stiffness degradation using fiber beam-column elements. The damage model was realized in Matlab by reading in the stress and strain of fibers, and the outputs of OpenSees. The validation of the damage model developed was illustrated on three RC columns and one RC plane frame that were tested under cyclic loading and seismic actions. On the basis of the study, the major conclusions obtained are as follows:

(1) The damage model developed can accurately determine the damage location, damage magnitude and damage evolution of RC columns as shown in the comparison between numerical simulation results and damage evolution process of two RC columns, and the comparison between the experimental results and damage evolution process of one RC column.

(2) The damage index increased rapidly at the early stage, and slowed down at the following stage. This is because the stiffness degradation of a structural member primarily results from the development of cracks at the early stage of loading, and then the stiffness degradation is influenced mainly by the compressive stress in the compression zone.

(3) Although both the damage model proposed in the study and inter-story drift can estimate story damage, the former may be more precise, especially for a structure with variable lateral inter-story stiffness, even a frail story.

(4) With the effective stiffness and effective area of a fiber as the basis for calculation, the model developed is enabled to estimate the damage states at the section, element, member, story and structure levels without introducing weighting coefficients or the corresponding force-displacement relationships. Additionally, for the same reason, the proposed damage model can accurately identify the damage at the story and structure levels by the direct stiffness method and static condensation method without introducing weighting coefficients.

The proposed damage model is proved to be a valuable and promising method for the analysis of the damage evolution of a structure at various levels in providing a solid foundation for predicting failure modes of a structure. Furthermore, the damage model has perfected the damage assessing function of OpenSees for RC members and structures, which should be conducive to damage estimation at different levels of

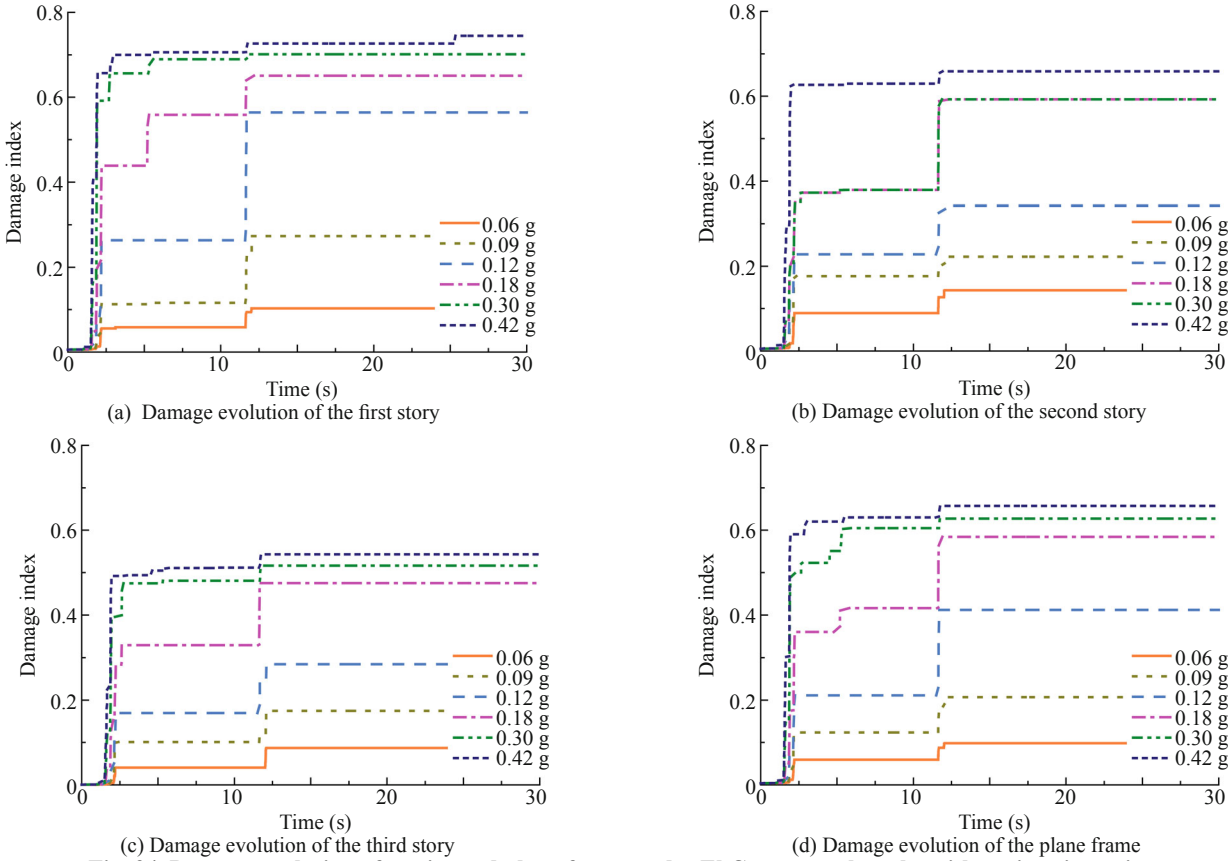

(a) Damage evolution of the first story
(b) Damage evolution of the second story
(c) Damage evolution of the third story
(d) Damage evolution of the plane frame

Fig. 34 Damage evolution of stories and plane frame under El Centro earthquake with various intensity

a large-scale structure under seismic action. However, several limitations of this study should be noted. The relationship between the compressive and tensile damage states and the effect of inelastic buckling of the longitudinal reinforced bars were not considered in this work. In addition to the enhanced damage models for concrete and reinforcing bars, the damage index-based limit state criterion should be determined to quantify the performance level in an RC structure under earthquake loading.

Acknowledgement

The generous support provided by the National Natural Science Foundation of China (Grant No. 51278218 and Grant No. 51078166) is gratefully acknowledged. The authors are especially grateful to Prof. Lu Xinzheng at Tsinghua University, for offering experimental data and photographs.

References

Amziane S and Dubé J-F (2008), "Global RC Structural Damage Index-based on The Assessment of Local Material Damage," *Journal of Advanced Concrete Technology*, **6**(3): 459–468.

Calabrese A, Almeida JP and Pinho R (2010), "Numerical Issues in Distributed Inelasticity Modeling of RC Frame Elements for Seismic Analysis," *Journal of Earthquake Engineering*, **14**(Sup1): 38–68.

Chang GA and Mander JB (1994), "Seismic Energy-based Fatigue Damage Analysis of Bridge Columns: Part I- Evaluation of Seismic Capacity," *NCEER-94-0006*,U.S. National Center for Earthquake Engineering Research, Buffalo, N.Y.

Chopra AK (1995), *Dynamics of Structures*, Prentice Hall, Upper Saddle River, N.J.

Dodd L and Restrepo-Posada J (1995), "Model for Predicting Cyclic Behavior of Reinforcing Steel," *Journal of Structural Engineering*, **121**(3): 433–445.

Ghobarah A (2001), "Performance-based Design in Earthquake Engineering: State of Development," *Engineering Structures*, **23**(8): 878–884.

Ghobarah A, Abou-Elfath H and Biddah A (1999), "Response-based Damage Assessment of Structures," *Earthquake Engineering & Structural Dynamics*, **28**(1): 79–104.

Heo Y (2009), "Framework for Damage-based Probabilistic Seismic Performance Evaluation of Reinforced Concrete Frames," *Ph.D. Thesis*, University of California, Davis, Ann Arbor, 201 pp.

Hindi RA and Sexsmith RG (2001), "A Proposed Damage Model for RC Bridge Columns under Cyclic Loading," *Earthquake Spectra*, **17**(2): 261–290.

Hsu TT and Mo Y-L (2010), *Unified Theory of Concrete Structures*, John Wiley & Sons, Hoboken.

Koh S and Stephens R (1991), "Mean Stress Effects on Low Cycle Fatigue for a High Strength Steel," *Fatigue & Fracture of Engineering Materials & Structures*, **14**(4): 413–428.

Kostic S and Filippou F (2012), "Section Discretization of Fiber Beam-column Elements for Cyclic Inelastic Response," *Journal of Structural Engineering*, **138**(5): 592–601.

Kunnath SK, El-Bahy A, Taylor AW and Stone WC (1997), "Cumulative Seismic Damage of Reinforced Concrete Bridge Piers," *Technical Report NCEER*, US National Center for Earthquake Engineering Research, Buffalo, 89–106.

Li G, Zhang Y and Li H (2013), "Seismic Damage Analysis of Reinforced Concrete Frame Using the Force Analogy Method," *Journal of Engineering Mechanics*, **139**(12): 1780–1789.

Li S, Zhai C and Xie L (2012), "Evaluation of Displacement-based, Force-based and Plastic Hinge Elements for Structural Non-linear Static Analysis," *Advances in Structural Engineering*, **15**(3): 477–488.

Li Z, Chen Y and Li N (2014), "A Damage Model for Reinforced Concrete Members Based on Material Damage," *Engineering Mechanics*, **31**(06): 53–59. (in Chinese)

Li Z, Teng J and He X (2011), "Seismic Damage Analysis Model for RC Structures Based on Concrete Plastic Damage Model," *Proceedings of the Structures Congress 2011*, Las Vegas, 2768–2779.

Lu X, Ye L, Pan P, Tang D and Qian J (2012a), "Pseudo-static Collapse Experiments and Numerical Prediction Competition of RC Frame Structure II: Key Elements Experiment," *Building Structure*, **42**(11): 23–26. (in Chinese)

Lu X, Ye L, Pan P, Zhao Z, Ji X and Qian J (2012b), "Pseudo-static Collapse Experiments and Numerical Prediction Competition of RC Frame Structure I: RC frame experiment," *Building Structure*, **42**(11): 19–22, 26. (in Chinese)

Maas S, Zürbes A, Waldmann D, Waltering M, Bungard V and De Roeck G (2012), "Damage Assessment of Concrete Structures through Dynamic Testing Methods. Part 1 – Laboratory Tests," *Engineering Structures*, **34**(2012): 351–362.

Mansour M, Lee J-Y and Hsu TT (2001), "Cyclic Stress-Strain Curves of Concrete and Steel Bars in Membrane Elements," *Journal of Structural Engineering*, **127**(12): 1402–1411.

Mazzoni S, McKenna F, Scott MH and Fenves GL (2006), *OpenSees Command Language Manual*, Pacific Earthquake Engineering Research (PEER) Center Berkeley.

Miner MA (1945), "Cumulative Damage in Fatigue," *Journal of Applied Mechanics*, **12**: A159–A164.

Park Y and Ang A (1985), "Mechanistic Seismic Damage Model for Reinforced Concrete," *Journal of Structural Engineering*, **111**(4): 722–739.

Saatcioglu M and Grira M (1999), "Confinement of Reinforced Concrete Columns with Welded Reinforced Grids," *ACI Structural Journal*, **96**(1): 29–39.

Teng J, Li Z, Ou J and He X (2011), "Fiber Damage Analysis Model for RC Beam-column Based on EEP Super-convergent Computation," *Science China Technological Sciences*, **54**(10): 2542–2548.

Tsuchiya S and Maekawa K (2006), "Cross-sectional Damage Index for RC Beam-column Members Subjected to Multi-axial Flexure," *Journal of Advanced Concrete Technology*, **4**(1): 179–192.

Van Paepegem W, Dechaene R and Degrieck J (2005), "Nonlinear Correction to the Bending Stiffness of a Damaged Composite Beam," *Composite Structures*, **67**(3): 359–364.

Waugh JD (2011), "Nonlinear Analysis of T-shaped Concrete Walls Subjected to Multi-directional Displacements," *Ph.D. Thesis*, Iowa State University, Ames, 294 pp.

Welfert B (2010), "A Note on Classical Gauss–radau and Gauss–lobatto Quadratures," *Applied Numerical Mathematics*, **60**(6): 637–644.

Xie L, Lu X, Guan H and Lu X (2015), "Experimental Study and Numerical Model Calibration for Earthquake-Induced Collapse of RC Frames with Emphasis on Key Columns, Joints, and the Overall Structure," *Journal of Earthquake Engineering*, **19**(8): 1320–1344.

Yazgan U and Dazio A (2012), "Post-earthquake Damage Assessment Using Residual Displacements," *Earthquake Engineering & Structural Dynamics*, **41**(8): 1257–1276.

List of symbols

$2N_{\mathrm{f}}$: Number of half-cycles to failure
$(2N_{\mathrm{f}})_k$: Number of half-cycles to failure at the strain amplitude $\varepsilon_{\mathrm{a},j}$ of the kth half-cycle
A_i: Initial area of the ith fiber
$\tilde{A}_i$: Effective area of the ith fiber
$A_{\mathrm{s},j}$: Cross-sectional area of the jth steel fiber without plastic deformation and fatigue damage
c: Fatigue ductility exponent
D_{c}: Concrete damage index
$\boldsymbol{d}_{\mathrm{member}}$: Rod-end deformations for a member
$\boldsymbol{d}_{\mathrm{sec}}(x)$: Section deformations
$\boldsymbol{d}_{\mathrm{story}}$: Story deformations
$\boldsymbol{d}_{\mathrm{structure}}$: Structure deformations
D_i: Damage value for the ith fiber
D_{member}: Damage index for a member
$D_{\mathrm{s},j}$: Damage index for the jth steel fiber
$D_{\mathrm{sec},k}$: Damage index for the kth section
D_{story}: Damage index for a story
$D_{\mathrm{structure}}$: Damage index for a structure
E_{c}: Initial tangent modulus of concrete
$E_{\mathrm{c},j}$: Initial tangent modulus of the ith concrete fiber
$\tilde{E}_{\mathrm{c},i}$: Initial reloading modulus of the ith concrete fiber
$\tilde{E}_{\mathrm{s},j}$: Initial reloading modulus of the jth steel fiber
E_i: Initial tangent modulus of the ith fiber
$\tilde{E}_i$: Initial reloading modulus of the ith fiber
$\boldsymbol{F}_{\mathrm{member}}$: Rod-end forces for a member and the rod-end deformations $\boldsymbol{d}_{\mathrm{member}}$
$\boldsymbol{F}_{\mathrm{sec}}(x)$: Section resisting forces
$\boldsymbol{F}_{\mathrm{story}}$: Story shears
$\boldsymbol{F}_{\mathrm{structure}}$: Structure shears
F_0, u_0, $\tilde{k}_{u_0,u_0}$: Force, displacement and effective lateral stiffness in the X direction at Node 0
F_n, u_n, $\tilde{k}_{u_n,u_n}$: Force, displacement and effective lateral stiffness in the X direction at Node n.
F_{px}, u_p, $\tilde{k}_{\mathrm{u}_p,\mathrm{u}_p}$: Force, displacement and effective rod-end stiffness in the X direction at Node p
F_{py}, v_p, $\tilde{k}_{v_p,v_p}$: Force, displacement and effective rod-end stiffness in the Y direction at Node p,
F_{qx}, u_q, $\tilde{k}_{\mathrm{u}_q,\mathrm{u}_q}$: Force, displacement and effective rod-end stiffness in the X direction at Node q
F_{qy}, v_q, $\tilde{k}_{v_q,v_q}$: Force, displacement and effective rod-end stiffness in the Y direction at Node q
$\tilde{\boldsymbol{f}}_{\mathrm{e}}(x)$: Effective element flexibility
f_{c}: Peak stress for unconfined concrete
f_s, u_s, $\tilde{k}_{u_s,u_s}$: Shear, displacement and effective lateral stiffness in the X direction at Node s
f_{s-1}, u_{s-1}, $\tilde{k}_{u_{s-1},u_{s-1}}$: Shear, displacement and effective lateral stiffness in the X direction at Node s-1
f_{un}^{-}: Unloading stress from the compression envelope curve
f_{un}^{+}: Unloading stress from the tension envelope curve
$\tilde{\boldsymbol{K}}_{\mathrm{e}}(x)$: Effective element stiffness
$\tilde{\boldsymbol{K}}_{\mathrm{member}}$: Effective member stiffness that has been condensed,
$\tilde{\boldsymbol{K}}_{\mathrm{sec}}(x)$: Effective section stiffness
$\tilde{\boldsymbol{K}}_{\mathrm{story}}$: Effective lateral stiffness for an equivalent story
$\tilde{\boldsymbol{K}}_{\mathrm{structure}}$: Effective lateral stiffness for an equivalent structure
k_n: Initial structure lateral stiffness corresponding to $\tilde{k}_n$
k_{u_s,u_s}, $k_{u_{s-1},u_{s-1}}$: Initial story lateral stiffness corresponding to $\tilde{k}_{u_s,u_s}$, $\tilde{k}_{u_{s-1},u_{s-1}}$.
$k_{\phi_{\mathrm{p}},\phi_{\mathrm{p}}}$, $k_{\phi_{\mathrm{q}},\phi_{\mathrm{q}}}$: Initial rod-end bending stiffness corresponding to $\tilde{k}_{\phi_{\mathrm{p}},\phi_{\mathrm{p}}}$, $\tilde{k}_{\phi_{\mathrm{q}},\phi_{\mathrm{q}}}$.

L : Length of a member

M_{p}, ϕ_{p}, $\tilde{k}_{\phi_{\mathrm{p}},\phi_{\mathrm{p}}}$: Bending moment, rotation and effective rod-end bending stiffness at Node p

M_{q}, ϕ_{q}, $\tilde{k}_{\phi_{\mathrm{q}},\phi_{\mathrm{q}}}$: Bending moment, rotation and effective rod-end bending stiffness at Node q

n: Number of half-cycles at which $D_{s,j}$ is computed

$n(x)$: Total number of fibers in a section

x_i : Location of the ith section

y_i : y coordinates of the ith fiber in the local-coordinate system

Z_{d}: Degradation constant

$\Delta\varepsilon$: Total strain range

ε_{a} : Strain amplitude

ε_{c} : Total concrete strain

$\varepsilon_{\mathrm{c}}^{\mathrm{p}}$: Plastic concrete strain

$\varepsilon_{\mathrm{cc}}$: Strain at the peak compressive stress

ε_{t} : Strain at the peak tensile stress

$\varepsilon_{\mathrm{crk}}$: Cracking strain in tension

$\varepsilon'_{\mathrm{f}}$: Fatigue ductility coefficient

$\varepsilon_{\mathrm{p},j}$: Plastic strain of the jth steel fiber

$\varepsilon_{\mathrm{sp}}$: Spalling strain in compression

$\varepsilon_{s,\max}$: Maximum strain in a cycle

$\varepsilon_{s,\min}$: Minimum strains in a cycle

$\varepsilon_{\mathrm{un}}^{-}$: Unloading strain from the compression envelope curve

$\varepsilon_{\mathrm{un}}^{+}$: Unloading strain from the tension envelope curve

$\lambda_{\mathrm{SR},j}$: Strength degradation factor for the jth steel fiber

σ_{c} : Concrete stress

ω_i : Quadrature weight of the ith section